Materials Advances

ROYAL SOCIETY OF CHEMISTRY

PAPER

View Article Online
View Journal | View Issue

Open Access Article. Published on 03 April 2024. Downloaded on 2/12/2026 8:17:39 AM.
This article is licensed under a Creative Commons Attribution 3.0 Unported Licence.

Check for updates

Cite this: *Mater. Adv.*, 2024, 5, 4187

Received 19th February 2024,
Accepted 19th March 2024

DOI: 10.1039/d4ma00168k

rsc.li/materials-advances

Fabrication of a room-temperature NO_2 gas sensor with high performance at the ppb level using an rGO/BiOCl heterostructure†

Neeraj Dhariwal,[a] Preety Yadav,[a] Amit Sanger,[a] Sung Bum Kang,[b] M. S. Goyat,[cd] Yogendra Kumar Mishra[d] and Vinod Kumar*[a]

In recent years, the continuous and accurate detection of human hazardous gases, such as NO_2, using a low-cost gas sensing device is quite important. For a new generation of gas sensors, rGO or 2-D materials have gained considerable attention. This work presents a low-temperature rGO/BiOCl heterojunction fabricated NO_2 gas sensor that exhibits an excellent response (R_g/R_a = 3.78) for NO_2 at 100 ppb compared to pristine BiOCl. The selected synthesis pathway results in the generation of a perforated floral morphology. Moreover, the sensor showed outperforming selectivity with a quick response/recovery of ∼9 s/21 s at ambient temperature (25 °C). Additionally, it has an ultralow LOD (∼0.06 ppb). Besides, the mechanism of gas sensing was initially elucidated through finite-difference time-domain (FDTD) simulation. This analysis confirms that rGO in BiOCl serves as a bridge, enhancing the transfer of electrons from BiOCl to NO_2 and resulting in a substantial increase in the depletion region and a heightened sensor response. Our fabricated NO_2 gas sensor offers a low gas detection limit with high accuracy and fast response at even lower temperatures.

1. Introduction

One of the most prevalent factors affecting human health is air pollution according to the World Health Organization (WHO).[1] Due to NO_2, NH_3, H_2S, CO_2, *etc.*, which are considered the most hazardous pollutants, the ambient environment becomes contaminated, which can lead to fatal conditions such as lung cancer, heart attack, strokes, skin allergies, asthma and neurological disorders.[2–6] Moreover, an upsurge in automobilization and industrialization has led to an enormous rise in the emissions of NO_2 gas, which is one of the most common hazardous gases. NO_2 released by industrial processes, vehicle exhaust and combustion endanger human health. The thinning of the ozone layer and the development of acid rain are some of the causes of NO_2, which affects aquatic, terrestrial and human lives.[7–9] Thus, NO_2 gas sensing equipment is in high demand.

Two-dimensional layered materials, such as graphene and MXenes, have been thoroughly studied owing to their high mechanical strength, excellent carrier mobility and high surface-to-volume ratio.[10–13] Numerous promising materials, including graphene and its derivatives, which have a larger surface area, are theoretically viable and can be used to detect gases. Additionally, their 2-D planar structure facilitates charge transport with brief diffusion paths. rGO has been widely used for gas sensor fabrication, which facilitates surface enhancement and functionalisation.[14–16] In contrast to graphene, rGO can increase adsorption energy and promote the adsorption of gases, which remains unaffected by orientation/sites. Consequently, rGO flakes have attracted attention as a potential component of gas-sensing materials.

Bismuth oxychloride, or BiOCl, is believed to be the most significant component of two-dimensional materials. It builds the [X–Bi–O–Bi–X] structure layer by layer and is joined by interlayered van der Waals forces and intra-layer bonding.[17] Because of its amazing structural, optical, and physiochemical qualities, this material has been used in various applications, including water filtration and catalysis.[18,19] However, this material has not been studied much in the realm of gas detection, especially NO_2. Semiconductor materials supported by rGO have been considered the most appropriate composite material for gas sensing devices because of the substantial amount of physisorption sites.[20,21] When combined with rGO, several common metal oxides, including ZnO, SnO_2, WO_3 and

---

[a] *Department of Physics, NSUT, Dwarka sec-3, New Delhi-110078, India. E-mail: vinod@nsut.ac.in*

[b] *Department of Materials Science and Engineering, University of Illinois at Urbana-Champaign, Urbana, IL, 61801, USA*

[c] *Department of Applied Science, School of Engineering, University of Petroleum and Energy Studies, Dehradun, 248007, Uttarakhand, India*

[d] *Mads Clausen Institute, SDU NanoSYD, University of Southern Denmark, Alsion 2, DK-6400, Sønderborg, Denmark*

† Electronic supplementary information (ESI) available. See DOI: **https://doi.org/10.1039/d4ma00168k**

© 2024 The Author(s). Published by the Royal Society of Chemistry

Open Access Article. Published on 03 April 2024. Downloaded on 2/12/2026 8:17:39 AM.
This article is licensed under a Creative Commons Attribution 3.0 Unported Licence.

CuO, demonstrated improved gas sensing capabilities compared to base metal oxides.[22–25] Despite this, the non-uniform hybridization between rGO and metal oxides leads to a ring-like deposition because particles are concentrated on droplet edges as a result of the coffee ring effect.[26,27] Consequently, the sensitivity and repeatability of the manufactured sensors are severely reduced.[28–32] Therefore, it was necessary to fabricate a novel and effective composite to detect NO_2 gas with high sensitivity along with the small size and ultrathin morphology of the rGO/BiOCl nanocomposite. The obtained structure can enhance the number of available active sites and electrical conductivity, which can further increase gas sensing performance. Thus, it is fascinating to investigate nanocomposites that exhibit strong selectivity towards NO_2 gas.[33]

In this regard, we fabricated heterogeneously assembled rGO flakes on semiconductor material, *i.e.* bismuth oxychloride. The rGO/BiOCl nanocomposites are synthesized using a one-step hydrothermal technique without any precipitating agent. The manufactured gas sensor has a high level of NO_2 gas selectivity and has minimal effect on humidity with remarkable sensitivity and excellent response/recovery time at room temperature (25 °C). The outstanding catalytic function of rGO and the charge transmission occurring between rGo flakes and BiOCl nanoflower account for this remarkable performance. Because rGO with a two-dimensional structure defines a large surface-to-volume ratio, more active sites are available. The accessible active sites are responsible for the catalytic activity of rGO, which improves sensor performance. Furthermore, rGO's electrical structure has a significant catalytic process conductive nature. In rGO, electron transport during catalytic processes is facilitated by sp^2 hybridised carbon atoms with delocalized pi-electrons. The kinetics of the catalytic process taking place on the rGO surface are improved by this electron mobility, which also strengthens the charge transfer mechanism. Simulation of rGO/BiOCl by finite difference time-domain confirms the improved build-in potential, leading to efficient gas detection sites when used as a gas sensor. The methodology proposed in this work could result in the development of a 2-D material/semiconductor hybrid NO_2 gas sensor with higher sensitivity.

2. Experimental section

2.1. Synthesis

A one-step hydrothermal process was used to yield BiOCl and rGO/BiOCl (see Fig. 1). To synthesize mesoporous floral, such as BiOCl, 6.58 g of Bismuth Nitrate ($Bi(NO_3)_3{\cdot}5H_2O$) (purity 98%, Merck) was dissolved in 19 mL of ethylene glycol, and 0.78 g sodium chloride (NaCl) (purity 99%, Sigma Aldrich) was dissolved in 3 mL de-ionized (DI) water and allowed to stir at 500 rpm for 30 min at 50 °C to form a homogeneous mixture. After that, both solutions were mixed thoroughly at 500 rpm for 1 h at 70 °C. Simultaneously, rGO along with DI water at different amounts (0–4 wt %) was allowed to ultrasonicate for 2 h. Afterwards, the rGO solution was mixed with a BiOCl solution for 1 h to attain a homogeneous mixture. Then, both the suspensions (*i.e.* containing rGO and BiOCl salt solution) were transferred into the autoclave and allowed to remain at 150 °C for 15 h. After obtaining precipitates, contaminants were removed by centrifuging them at 8000 rpm and rinsing them several times with DI. Prior to drying in a vacuum oven at 100 °C for 24 h to obtain floral, such as BiOCl and rGO/BiOCl.

2.2. Gas sensing setup

A well-defined experimental setup contributes valuable insights into the gas sensing field. Fig. 2 illustrates the sensing setup used for this study. The setup includes a robust design for valuable and accurate measurements. The experimental setup includes a gas sensing chamber of 3 mL volume in which a controlled amount of NO_2 is purged with precise measurement and standard instruments to monitor the gas level. NO_2 gas (Sigma Aldrich, 1 ppm, with dry air used for balancing gas concentration) was combined with dry air using two Mass Flow Controllers (MFCs, MF-3000), which were further inserted into

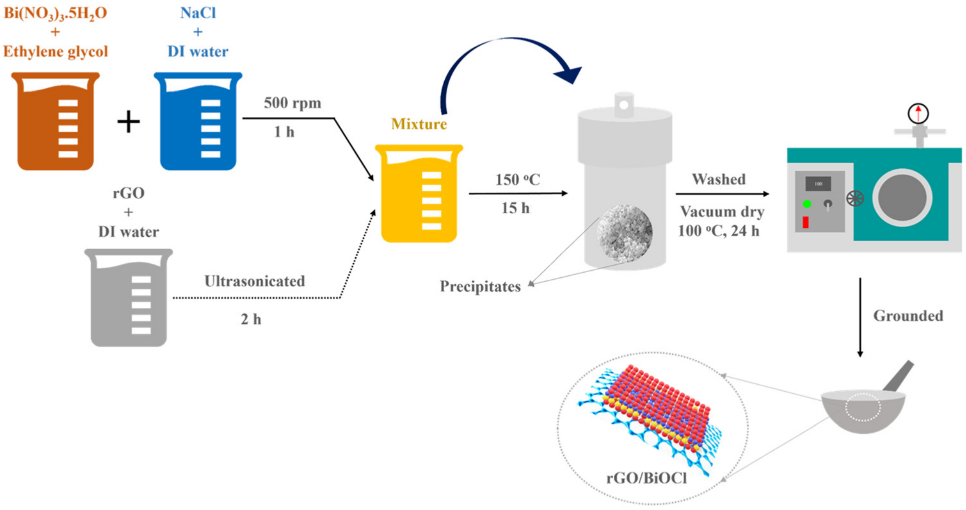

Fig. 1 Synthesis route for rGO/BiOCl heterostructure.

© 2024 The Author(s). Published by the Royal Society of Chemistry

Open Access Article. Published on 03 April 2024. Downloaded on 2/12/2026 8:17:39 AM.
This article is licensed under a Creative Commons Attribution 3.0 Unported Licence.

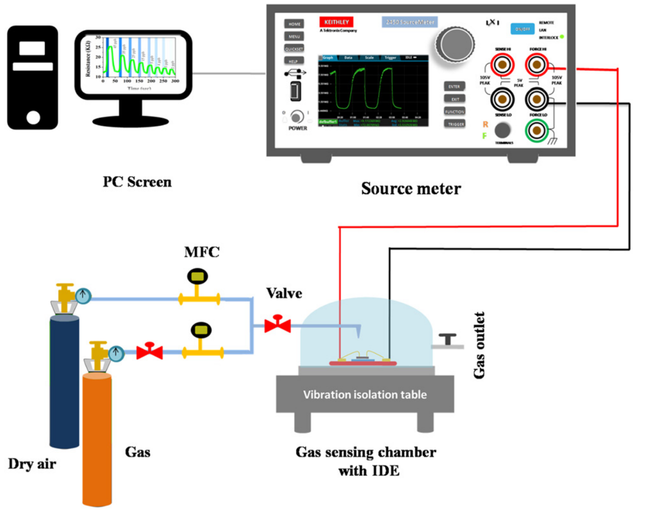

Fig. 2 Illustration of the gas detection system.

the gas sensing chamber with the desired gas concentration. Further, the gas flow rate was set at 100 SCCM. Additionally, an IDE comprising advanced sensing material was placed within the chamber to keep track of and evaluate the gas interactions. Gas sensing setup includes a Keithley 2450 source meter for real-time detection of sensor response towards varying NO_2. All these measurements are performed under a controlled environment and a room temperature of 25 °C.

2.3. Sensor fabrication

There are numerous effective methods for the deposition of nanoparticles, which have been employed for required monolayer and multilayer colloidal crystal processes.[34] Because the spin coating technique is flexible, affordable, and easy to fabricate, we chose it for the creation of single-layered colloidal-based sensors. Initially, the surface of the electrodes was cleaned with hexane and anhydrous ethanol, which were further desiccated for 1 h at 60 °C. The 10 mg synthesized BiOCl and rGO/BiOCl were initially dispersed in 1 mL ethanol, followed by spin coating over interdigitated electrodes (IDE), as shown in Fig. 3, at 4000 rpm for 1 min, then dried for 30 min at 80 °C and was further used for NO_2 sensing.

2.4. Characterization

The formulation, phase, and generated strain of the synthesized nanoparticles were examined by X-ray diffraction within a 2θ range from 20° to 80° using Cu-kα radiation. The morphology and interfacial structure of the synthesized samples were envisioned using a scanning electron microscope (SEM) with elemental mapping. Raman spectroscopy was employed to understand the structural characteristics of the synthesized materials. UV-Vis spectrometry and dielectric measurements were performed to better understand the electronic and optical properties. The total surface area and pore volume of BiOCl and rGO/BiOCl were measured using BET. To investigate the manufactured sensor's reaction to NO_2 gas, *I–V* characterization was performed. Specific environmental conditions were maintained in the test chamber for the sensor device.

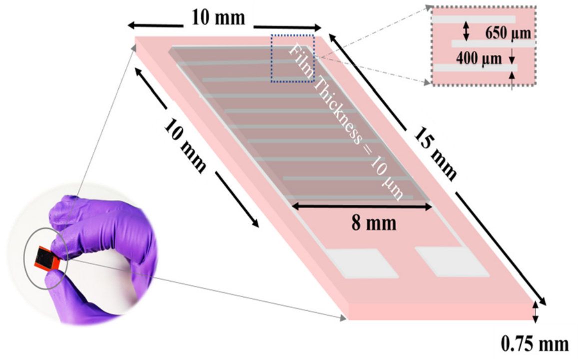

Fig. 3 Thin film-based sensor fabrication over IDE.

3. Results and discussion

3.1. Structural evaluation

Fig. 4(a) shows the XRD peaks of the synthesized BiOCl and rGO/BiOCl nanoparticles. The peak position along with the corresponding planes matches the JCPDS number 06-0249, confirming the proper phase formation. The observed pattern demonstrates that the peaks of rGO/BiOCl shift along with the broadening of the peaks, which is due to changes in lattice parameters and the strain developed between the bonds. Analysis of the data yielded the tetragonal structure, and the crystallinity was determined using the Debye Scherer formula[35]:

$$D = \frac{k\lambda}{\beta\cos\theta}, \tag{1}$$

where k represents the Scherer's constant, *i.e.* 0.9; λ denotes the wavelength of Cu-kα radiations; and β and θ denote FWHM and Bragg's angle, respectively. Moreover, the lattice constant was examined by applying eqn (2):

$$d_{hkl} = \frac{1}{\sqrt{\frac{h^2+k^2}{a^2}+\frac{l^2}{c^2}}}, \tag{2}$$

where d_{hkl} is used to represent interplanar spacing, which can be determined with Eqn (3):[36]

$$d_{hkl} = \frac{\lambda}{2\sin\theta}. \tag{3}$$

Further, the X-ray density (ρ_{XRD}) for BiOCl and rGO/BiOCl is examined by employing eqn (4):[37,38]

$$\rho_{XRD} = \frac{ZM}{Na^3}, \tag{4}$$

where Z and N denote the number of molecules per unit cell and Avogadro number, respectively, and M and a^3 represent the molecular weight and volume of the unit cell, respectively. Additionally, the mass of the sample (m) and its volume (V) were used to calculate bulk density (ρ_{exp}), as indicated by Eqn (5):[39]

$$\rho_{exp} = \frac{m}{V}. \tag{5}$$

The measured values of both ρ_{XRD} and ρ_{exp} are demonstrated in Table 1, indicating that X-ray density increases for

Open Access Article. Published on 03 April 2024. Downloaded on 2/12/2026 8:17:39 AM.
This article is licensed under a Creative Commons Attribution 3.0 Unported Licence.

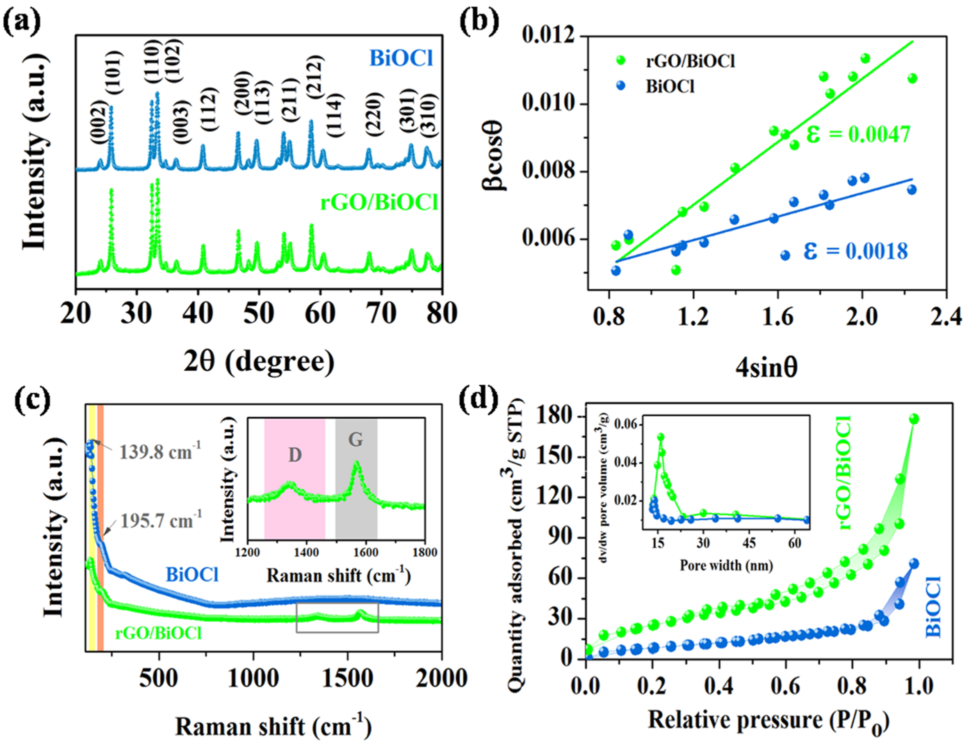

Fig. 4 (a) XRD peaks pattern, (b) Williamson–Hall plot, (c) Raman spectra and (d) N_2 sorption isotherm for pristine BiOCl and rGO/BiOCl along with the pore size distribution curve (inset).

rGO/BiOCl, which is the primary reason why synthesized samples have porosity, and the porosity was calculated using the following formula:[40]

$$P = 1 - \frac{\rho_{\mathrm{exp}}}{\rho_{\mathrm{XRD}}}. \tag{6}$$

We can recognize the difference in both densities in Table 1. The variation in densities in the samples is related to porosity, which may explain the existence of pores in the synthesized materials.

Additionally, the Williamson–Hall plot between $\beta\cos\theta$ and $4\sin\theta$ was used to determine the strain developed by forming a nanocomposite using eqn (7):[41]

$$\beta\cos\theta = \frac{k\lambda}{D_{\mathrm{WH}}} + 2\varepsilon\sin\theta, \tag{7}$$

Where ε represents the generated strain in the material and $\frac{k\lambda}{D_{\mathrm{WH}}}$ represents the intercept of the fitted line. The W–H plot for BiOCl and rGO/BiOCl has been shown in Fig. 4(b), exhibiting a rising trend in the strain after modification by rGO, which is due to dislocation formation at the interface between rGO and BiOCl when rGO is added to BiOCl. These dislocations simultaneously cause an increase in lattice strain and serve as a focus of concentration for stress. Additionally, fluctuation in bond length and bond angle of Bi–O and Bi–Cl could generate lattice strain.[42–44]

Table 1 Parameters calculated using XRD

Sample	Crystallite size (nm)	ρ_{XRD} (g cm^{-3})	ρ_{exp}	Porosity (P)	Strain (ε)
BiOCl	28.8	21.1	4.2	0.79	0.0018
rGO/BiOCl	25.7	27.3	2.2	0.91	0.0047

3.2. Raman spectroscopy

When examining the structural characteristics of carbon present materials, Raman spectroscopy is a vital tool. The Raman spectra of rGO/BiOCl and BiOCl are displayed in Fig. 4(c). Pure BiOCl is represented by the tetragonal structure of space group $P4/nnm$ with A_{1g}, B_{1g}, E_{g1} and E_{g2} acting as its four active modes.[45] Two prominent bands are observed in the BiOCl spectrum. The bands at 139.8 cm^{-1} and 195.7 cm^{-1} are assigned to A_{1g} and E_{g1} stretching modes between Bi–Cl. All Raman bands of BiOCl are observed in the rGO/BiOCl sample. The D and G bands are two separate peaks located at 1345 cm^{-1} and 1570 cm^{-1}, respectively, observed in rGO/BiOCl, which confirms the rGO presence.[46] The D band is attributed to defects, disorders and edges. The G band is formed by graphite's well-ordered sp^2 carbon, which arises from the zone center E_{2g} mode. According to the Raman spectra of rGO/BiOCl, the D and G bands are highly intense, suggesting an increment in sp^2 domain size and further verifying the brittleness of oxygen atoms, which is favourable for gas sensing.[47,48] Moreover, the rGO/BiOCl sample showed that all the rGO Raman bands were present, as indicated, demonstrating the successful creation of rGO/BiOCl.

© 2024 The Author(s). Published by the Royal Society of Chemistry

Open Access Article. Published on 03 April 2024. Downloaded on 2/12/2026 8:17:39 AM. This article is licensed under a Creative Commons Attribution 3.0 Unported Licence.

3.3. N_2 sorption isotherm

Using the nitrogen-sorption isotherm, the precise surface properties and pore volume of the synthesized nanomaterials were determined, and the results are shown in Fig. 4(d). The BiOCl/rGO nanocomposite is categorized as a type II isotherm by IUPAC with an H3-type hysteresis loop, having a wide variety of pore sizes, which suggests the presence of a mesoporous structure.[49] The volume of pores present in rGO/BiOCl increases by 4 times, *i.e.* 0.148 $cm^3\ g^{-1}$ in comparison to 0.037 $cm^3\ g^{-1}$ (BiOCl), and the average pore size increases to 15.7 nm from 12.6 nm, resulting in the highly porous nature of synthesized rGO/BiOCl. Based on calculations, the specific area of the surface of rGO/BiOCl was found to be 68.72 $m^2\ g^{-1}$, which is approximately 5 times higher than that of BiOCl (13.19 $m^2\ g^{-1}$). More active sites that facilitate gas adsorption and reaction during sensing may be available on a larger attainable surface area, allowing for a quicker response and improved sensitivity.[50,51]

3.4. Morphological analysis

The interfacial structure, morphology and composition of BiOCl and rGO/BiOCl nanoparticles were evaluated by SEM (scanning electron microscopy). Fig. 5(a) displays the BiOCl SEM images, which suggest that the synthesized BiOCl was composed of a perforated floral-like hierarchical structure with uniform width and thickness. According to Fig. 5(b), the as-synthesized BiOCl and rGO are evenly mixed in the nanocomposite, and the crinkled rGO thin layers firmly adhere to the BiOCl's outer layer to form an intact hybrid heterojunction. Furthermore, a rGO/BiOCl nanocomposite exhibits relatively smaller and thinner flakes of the perforated flower than BiOCl. This may be due to the introduction of rGO into the precursor, which provides nucleation sites in which BiOCl can form and prevent crystal growth.[52]

Furthermore, rGO/BiOCl nanocomposites provide an active surface modification position for BiOCl due to the rGO's oxygen comprising functional groups, which results in a more regular shape than pure BiOCl.[53] It also experiences strain, demonstrated by the W–H plot, indicating the reason behind lattice distortion, which comparatively increases porosity and the surface-to-volume ratio. Because of the additional voids created by the rGO/BiOCl nanocomposite, there are more active sites that improve NO_2 gas detection. Elemental distribution is examined by elemental color mapping (see Fig. 5), which validates the successful formation of rGO/BiOCl nanocomposite.

3.5. Electronic and optical properties

The band structure of pristine BiOCl and rGO/BiOCl is shown in Fig. 6(a), which demonstrates the band gap energy by applying a Tauc plot using the Tauc relation:[54]

$$(\alpha h\nu)^2 = (h\nu - E_g), \tag{8}$$

Where α, h and ν denote absorption co-efficient, Plank's constant and frequency, respectively. Moreover, E_g denotes the material's band gap energy.

Pristine BiOCl displays a band gap value of 3.7 eV. Furthermore, rGO leads to a reduction of energy to 3.1 eV when added to BiOCl by transferring electrons to the Fermi level. In the case of rGO/BiOCl, the electronic structure is disturbed due to addition of rGO to BiOCl, which creates an additional number of energy states within the band structure, resulting in a reduced band gap. In contrast, rGO plays an important role in introducing new pathways for charge carriers, which leads to a decrease in the band gap and an increase in conductivity. Additionally, the chemical interaction between the bands of Bi–C has a significant effect on the charge transfer property. To better understand the electrical conductivity of BiOCl and rGO/BiOCl, an impedance study was conducted. As shown in Nyquist plots (see Fig. 6(b)) for BiOCl and rGO/BiOCl, heterojunction shows a small diameter of the semicircle, indicating a higher charge transfer property with lower resistance.[55]

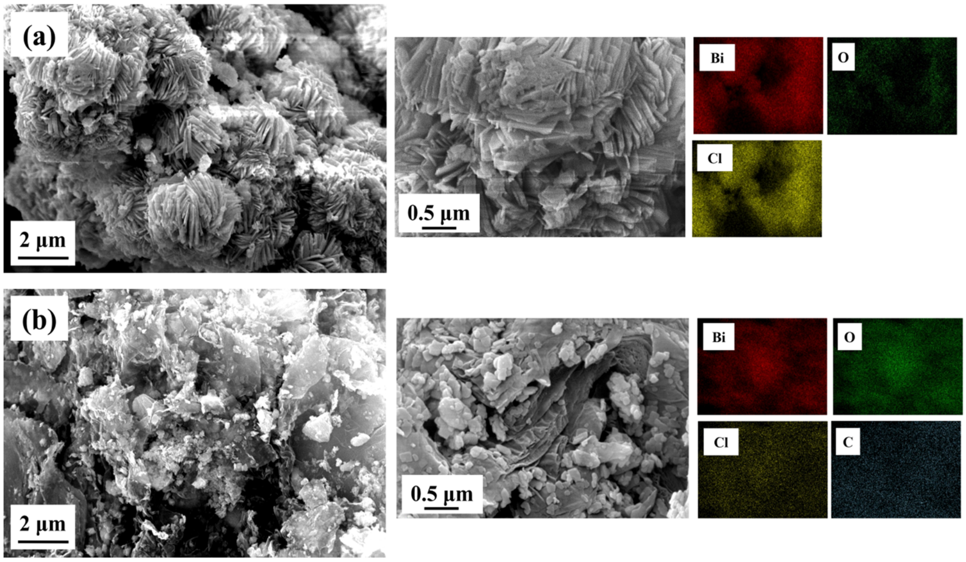

Fig. 5 Obtained morphology of (a) pristine BiOCl and (b) rGO/BiOCl along with elemental mapping using SEM.

Open Access Article. Published on 03 April 2024. Downloaded on 2/12/2026 8:17:39 AM.
This article is licensed under a Creative Commons Attribution 3.0 Unported Licence.

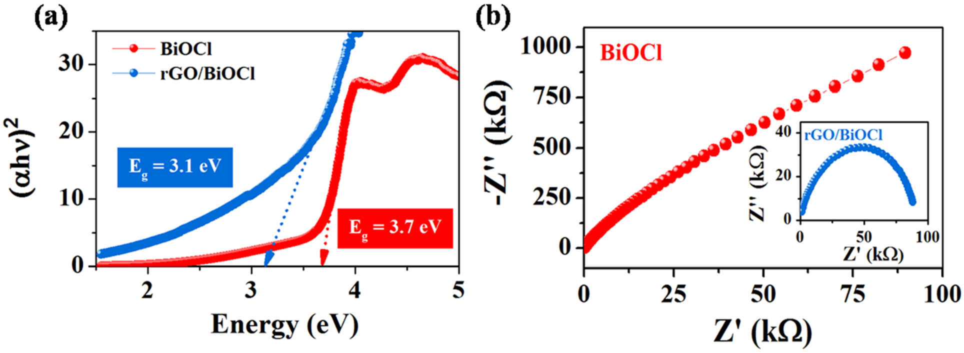

Fig. 6 (a) Tauc plot and (b) EIS spectra for pristine BiOCl and rGO/BiOCl.

The results revealed that the synergistic effect arising from the heterojunction of rGO/BiOCl significantly augmented the electron mobility of the system.

3.6. Gas sensing performance

The sensing capability of both fabricated BiOCl and rGO/BiOCl (see Fig. 7(a)) was performed under a controlled environment at a room temperature of 25 °C. As illustrated in Fig. 7(b), when the fabricated sensor comes into contact with NO_2, sensor resistance increases, indicating n-type sensor behavior. Initially, BiOCl was tested under the NO_2 gas exposure of 100 ppb, as shown in Fig. 7(b).

The sensor responded within $\tau_{res} = 35$ s, while $\tau_{rec} = 57$ s with a sensor response of $\frac{R_g}{R_a} = 1.72$,[56] which is calculated using the following formula:

$$\text{Response} = \frac{R_g}{R_a}, \tag{9}$$

where R_g and R_a are the resistances of the sensor in the presence of gas and air, respectively.

Interestingly, rGO/BiOCl heterojunction shows excellent enhancement in sensor response, *i.e.* $\frac{R_g}{R_a} = 3.78$, with quick reaction time ($\tau_{res} = 9$ s) and restoration/recovery time ($\tau_{rec} = 21$ s) for 100 ppb at room temperature (see Fig. 7(c)); additionally, response/recovery times at different NO_2 concentrations are studied (see Fig. S1, ESI†). With the addition of rGO to BiOCl, the material becomes more conductive, thereby facilitating the kinetics of charge transfer while reacting with gas. The elevation in electrical conductivity yields a rapid and enhanced sensor response. Additionally, a fabricated heterojunction structure may suppress the rate of recombination of generated charge carriers while interacting with NO_2 gas, leading to more variation in electrical conductivity and, henceforth, higher sensor response. Furthermore, the addition of rGO enhanced the sensor's specific surface area, generating more active gas interaction sites. The sensor displays higher sensitivity and remarkable repeatability, as displayed in Fig. 7(d). The primary cause of the sensor's amazing performance is the conductive bridge formed due to rGO stacking using BiOCl with its porous nature and higher surface area. Moreover, the fabricated sensor tested up to a

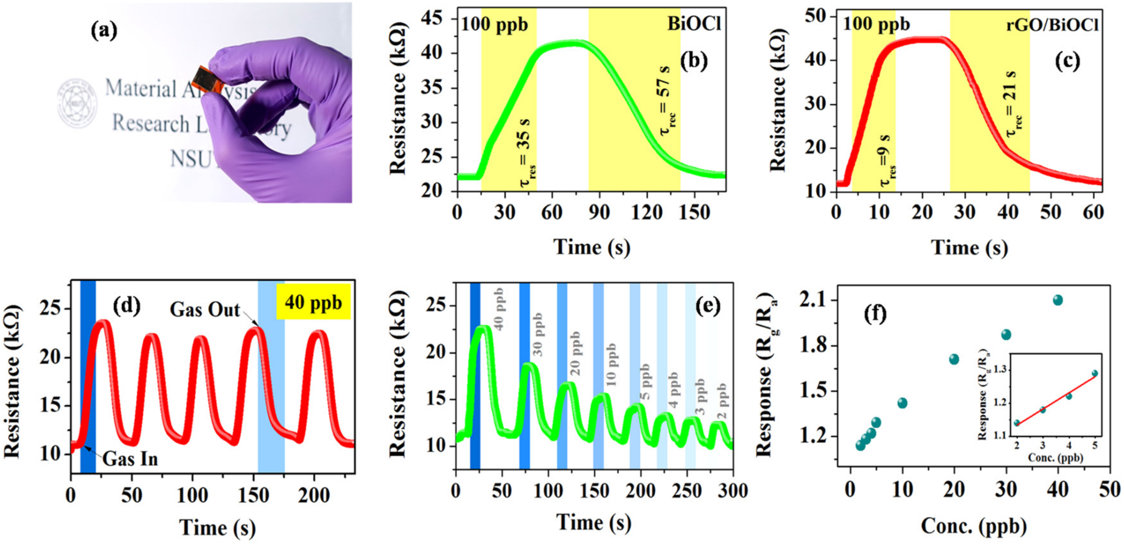

Fig. 7 (a) Thin film deposited over IDE, (b) and (c) response curve for BiOCl and rGO/BiOCl, (d) sensing repeatability curve for rGO/BiOCl, (e) variation in sensor response with different ppb levels and (f) the limit of detection for rGO/BiOCl.

© 2024 The Author(s). Published by the Royal Society of Chemistry

Open Access Article. Published on 03 April 2024. Downloaded on 2/12/2026 8:17:39 AM.
This article is licensed under a Creative Commons Attribution 3.0 Unported Licence.

low detection limit of 2 ppb (see Fig. 7(e) and Fig. S2, ESI†); theoretically, the value was obtained to be ultralow, *i.e.* 0.06 ppb (see Fig. 7(f)). The linear fit for the sensor response with ppb shows a resultant slope of 0.049 with a 0.99 value of R^2.

Variation in rGO concentration (0.5–4 wt%) in BiOCl was also tested, as shown in Fig. 8, which does not exhibit a monotonically straightforward trend. Initially, at lower concentrations of rGO, it leads to the enhancement of the sensing properties along with its electrical conductivity up to a certain threshold, and the further addition of rGO content leads to diminishing results and adverse effects on sensing parameters. This is possibly due to the agglomeration of rGO sheets and an alternating decrease in active sites, which can alter the interaction between NO_2 gas and material. However, the formation of a local junction enhances the depletion region; moreover, the conduction channel shifts to linked rGO flakes due to higher conductivity and simultaneously lower sensor resistance. Therefore, a higher response at 2 wt% is due to the well-dispersed rGO flakes.

Selectivity is one of the salient features of any gas sensor studied by the behavior of gas with the sensor surface.[57–59] Various gases, including NO, CO_2, CH_4, H_2, H_2S, NH_3 and NO_2, were tested, while the sensor best responded to NO_2 with a response of 3.78 times (see Fig. 9(a)). The electronic configuration and sensor surface characteristics of heterojunctions create preferential binding sites for NO_2 gas molecules, promoting the specific interaction of NO_2 gas with the sensor, which leads to enhanced sensitivity compared to other gases. The impact of humidity on sensor response was investigated to learn more about the environmental effect, as shown in Fig. 9(b).[60] Artificial humidity was created inside the gas chamber. It is clear from the obtained results that the sensor response gradually reduced by 12% with an increased humidity of 90%. Water vapours at high humidity hinder gas molecules from reacting with the sensor surface or thwarting the process of chemisorptions.[61] In contrast, the sensor response was carried out at varied temperatures (near environmental temperature).[62] Fig. 9(c) illustrates how an increase in temperature is linked to an increase in sensor response because of an increase in the quantity of surface electrons. The sensor also responded even at temperatures below RT although the sensor response was less at 0 °C. The diffusion rate of (NO_2) gas through the material at lower temperatures is quite slow, which reduces contact with the active sites and, correspondingly, the sensor response. Fig. 9(d) shows the stability of the rGO/BiOCl-based sensor towards NO_2 at 100 ppb for a long time.[63] Fig. 9(d) demonstrates a total decrease of 4% in the sensor response after 25 days. These studies suggest that the incorporation of superior performance and mixed dimensional gas sensors, coupled with a better understanding of underlying mechanisms, could lead to new possibilities in hybrid sensor platforms based on 2D materials.

3.7. Gas sensing mechanism

Fig. 10 illustrates the rGO/BiOCl-based sensing mechanism towards NO_2 gas, where the rGO/BiOCl sensor works on the adsorption mechanism. Initially, ionization of oxygen molecules occurs at the sensor surface, extracting surplus electrons and simultaneously inducing alteration in both carrier concentration (N_d) and formation of a potential barrier (qV_{s1}). Temperature also plays a role in the type of adsorbed oxygen.[64] Elevation in the vertical position of qV_{s1}, further to qV_{s2} with NO_2 exposure results in the subsequent reduction in the electric current.

$$O_{2(air)} \rightarrow O_{2(ads)} \tag{10}$$

$$O_{2(ads)} + e^- \rightarrow O_{2(ads)}{}^- \tag{11}$$

$$O_{2(ads)}{}^- + e^- \rightarrow 2O_{(ads)}{}^- \tag{12}$$

$$NO_2 + 2O_{(ads)}{}^- \rightarrow NO_2{}^- + O_{2(ads)}{}^- \tag{13}$$

Thus far, charge transport through heterojunction can only be simplified using numerical, but sensing performance with charge transportation can be explained easily using Fig. 10. The same is applied to the transduction function of the heterojunction-based sensor. Using eqn (14) and (15), the effect of the heterojunction on

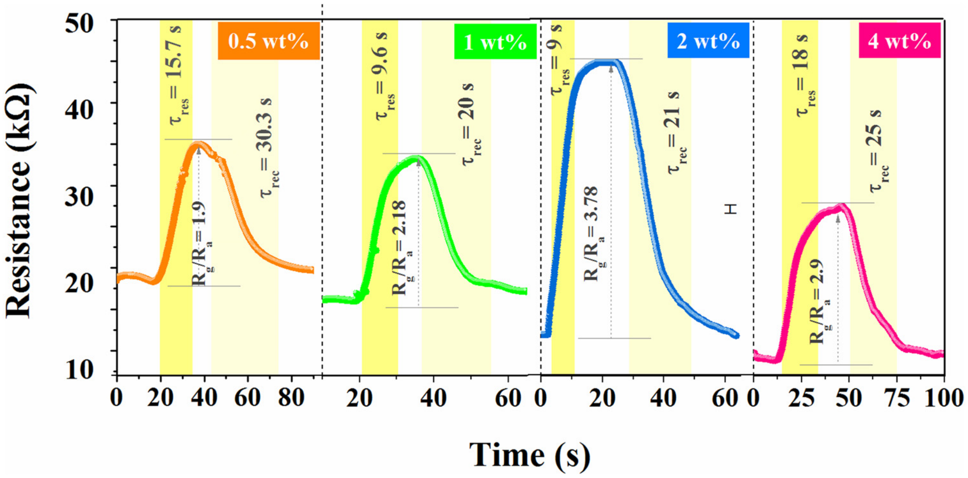

Fig. 8 Effect on NO_2 sensing behavior with variation in rGO concentration (0.5–4 wt%).

Open Access Article. Published on 03 April 2024. Downloaded on 2/12/2026 8:17:39 AM.
This article is licensed under a Creative Commons Attribution 3.0 Unported Licence.

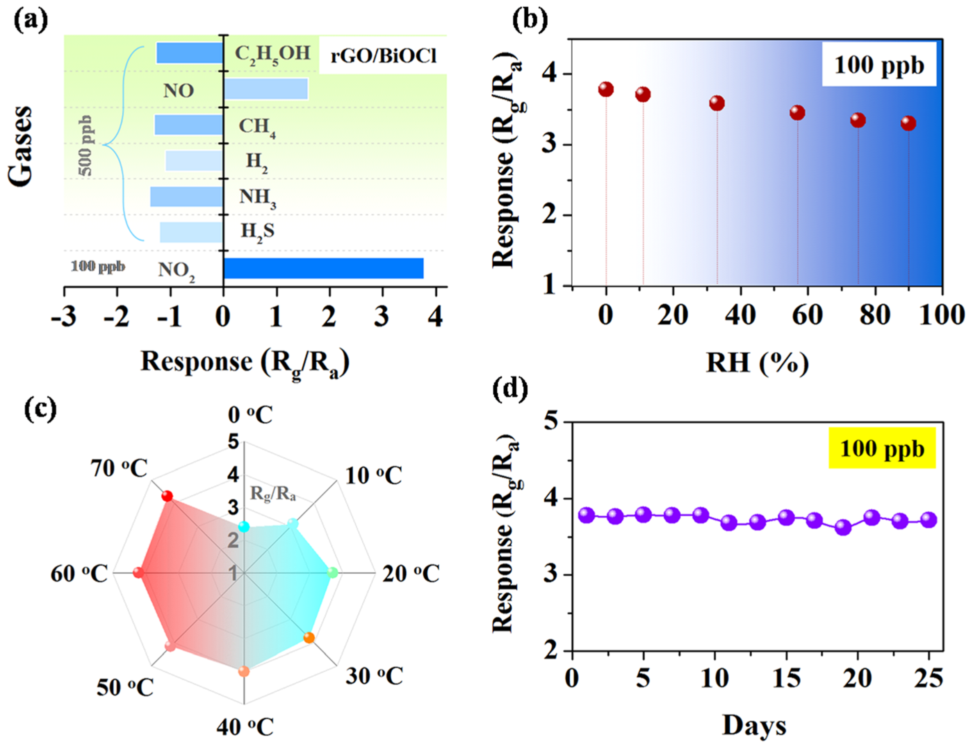

Fig. 9 (a) Sensor's selectivity using various gases, (b) the effect of humidity, (c) the effect of temperature and (d) the long-duration stability of the rGO/BiOCl-based sensor.

sensor performance with charge transport properties can be easily studied by measuring the height difference in the potential barrier.[65] The charge transport property between the overlapping particles is modulated by adsorbate-induced variation in the height of the potential barrier ΔV_s at the junction. Electron mobility within the junction region can be explained by thermo-electronic emission.[66] The sensing response is contingent upon the adsorbate-induced fluctuating height of the potential barrier, which can be defined as follows:

$$V_s = \frac{2\pi Q_s{}^2}{\varepsilon N_d} = \frac{2\pi (qN_s)^2}{\varepsilon N_d}, \tag{14}$$

$$\text{Response} = \frac{R_g}{R_a} \approx \exp\left(\frac{e\left(\dfrac{V_{s2}}{V_{s1}}\right)}{kT}\right), \tag{15}$$

where e, Q, k, T and ε are the elementary charge, surface charge density, Boltzman constant, operating temperature and dielectric constant, respectively. Therefore, flakes of rGO along with the associated functional group of oxygen can modulate potential barriers, which is advantageous for improving the response of gas sensing. Moreover, the enhanced point defects on the heterojunction of rGO/BiOCl provide more surface for adsorption of NO_2 gas and a more effective sensor response when compared to previously published NO_2 gas sensors (see Table 2).

The work functions of rGO (Φ = 4.75 eV) and BiOCl (Φ = 7.35 eV) allow for the formation of the Schottky junction, which additionally creates a bridge for the exchange of electrons from BiOCl to rGO. Initially, the interaction of the sensor surface with the oxygen molecule forms oxygen ion species when the heterojunction composed of rGO/BiOCl is subjected to air (see Fig. 10). However, in the NO_2 environment, adsorption of gas molecules occurs, which preferentially interacts with the chemisorbed oxygen present. The adsorbed molecule of NO_2 gas entails the sequestration of electrons from O^- and O^{2-} ions present on the surface. Consequently, the greater number of electrons consumed is there to produce chemisorbed oxygen species and, henceforth, fewer electrons in rGO/BiOCl. Therefore, the region of depletion and the height of the barrier enlarge; correspondingly, sensor resistance increases (see Fig. 10).

The propensity of rGO flakes to undergo self-aggregation and self-connection is observed. The aforementioned effect continues to facilitate the development of a depletion layer over BiOCl despite the presence of local junctions. Interestingly, because of their significantly higher conductivity, the conduction pathway partially shifts towards interconnected rGO flakes, which reduces the sensor resistance. The depletion region widens when the fabricated sensor is exposed to NO_2 gas; however, the resistance change or resultant response is not noticeable due to well-connected rGO flakes, which allow easy charge transfer. Consequently, a boost in the sensor's response is elucidated as a result of the advantageous impact of evenly distributed rGO flakes. To better understand the sensing mechanism and to design a more sensitive gas sensor, FDTD simulation is used based on the Crowell-size model and the drift Diffusion–Poisson equation at the interface to determine the distribution of electric potential with rGO. We observed that

© 2024 The Author(s). Published by the Royal Society of Chemistry

Open Access Article. Published on 03 April 2024. Downloaded on 2/12/2026 8:17:39 AM.
This article is licensed under a Creative Commons Attribution 3.0 Unported Licence.

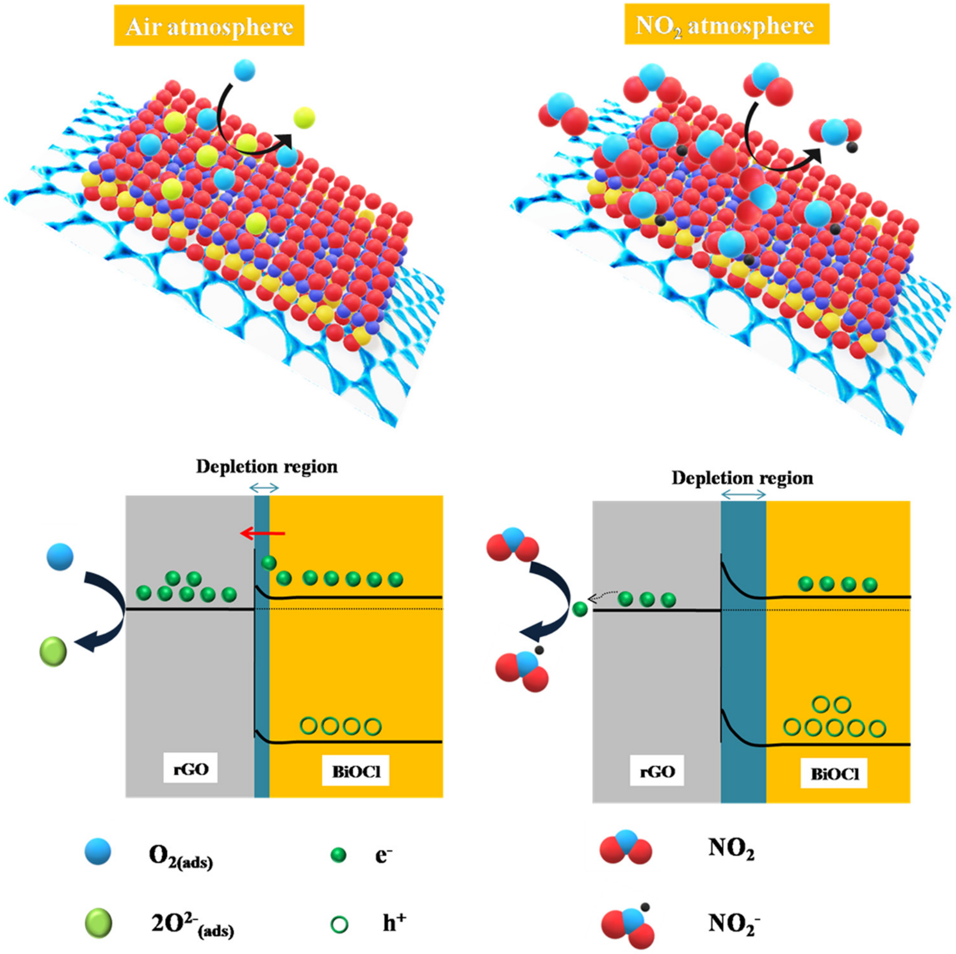

Fig. 10 rGO/BiOCl-based fabricated sensor mechanism in the presence of air and NO_2.

Table 2 Properties of previously studied NO_2 gas sensors

Materials	Conc. (NO_2)	τ_{res}/τ_{rec} (s)	Sensitivity/ response	Ref.
SnS_2	10 ppm	170/140	36.33	67
rGO	10 ppm	71/310	21.56%	68
WSe_2 nanoflakes	0.05 ppm	50/1050	5.06%	69
MoS_2	100 ppm	71/310	21.56%	70
rGO-SnS_2	5 ppm	50/48	32	71
Fe_2O_3@rGO	100 ppb	100/—	1.23	72
ZnO-rGO	5 ppm	165/499	25.6%	73
In_2O_3@rGO	500 ppb	4.2/13.3 min	15%	74
Co_3O_4-rGO	60 ppm	—/—	80%	75
rGO-BiOCl	100 ppb	9/21	3.78	This study

the NO_2 gas molecules became closer to the top view of the platform. The field of electric potential can be observed, which deteriorates the sensing execution of the fabricated sensor (see Fig. 11).

BiOCl has a wide band gap that limits sensor sensitivity under normal ambient light at RT. In contrast, the lower conductivity of BiOCl compared to rGO results in less efficient charge transfer and a slower sensor response. Further, when rGO/BiOCl interacts with electrophillic NO_2, transfer of electrons from rGO/BiOCl to NO_2 occurs, leading to a decrease in BiOCl carrier concentration, and this is why the potential barrier also increased linked with the wider depletion region. The increased sensor response has multiple causes. Firstly, in heterojunctions, such as rGO/BiOCl, specifically 2 wt% rGO, an inversion layer may form at the interface because of the different work functions and band alignments of the two materials. Secondly, electrons and holes are effectively separated in a heterojunction where the

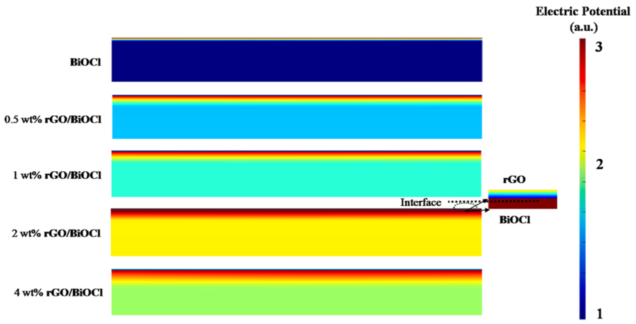

Fig. 11 FDTD simulated based electric potential for different wt% (0–4 wt%) rGO/BiOCl.

Open Access Article. Published on 03 April 2024. Downloaded on 2/12/2026 8:17:39 AM. This article is licensed under a Creative Commons Attribution 3.0 Unported Licence.

conduction band of one material is shorter compared to the valence spectrum of the other. This separation is necessary to enhance the sensor sensitivity.[76–81] The pronounced build-in potential in the vicinity of the rGO/BiOCl heterojunction interface results in the formation of a significant depletion layer and a long range of coulomb interaction is generated. Interestingly, the increase in electric potential at the interface also augments the force of electrostatics within, indicating the active role of rGO in NO_2 sensing as a catalytic agent. However, after a certain level (>2 wt%), it shows higher conductivity, which in turn leads to a low level of modulation between the rGO and BiOCl interface, further deteriorating the sensor's sensing performance. These results match well with the experimental data.

4. Conclusions

In the present investigation, we delineate the conceptualization and fabrication of an ultrasensitive sensor to monitor NO_2 gas in the environment. The rGO/BiOCl-dependent gas sensing material was created using a straightforward, one-step hydrothermal process, which was further coated over IDE using the spin coating technique. The heterojunction rGO/BiOCl sensor achieved an excellent response of 3.84 times with quick response/recovery time (τ_{res}/τ_{rec}= 9 s/21 s) at RT (25 °C). Moreover, this developed sensor has ultralow theoretical LOD ($\sim$0.06 ppb) and long-term durability. The pivotal rise in the sensor's performance is attributed to the rGO flakes providing chemisorption sites for oxygen molecules. One of the major factors is the Schottky junction formed between rGO and BiOCl, which further promotes the transport of charge carriers to the NO_2 gas molecules. This phenomenon actively contributes to rising sensing dynamics, as observed in the system. The elucidation of the sensing mechanism is done initially using FDTD simulation. The outcome of the aforementioned study clarifies that the presence of rGO in rGO/BiOCl facilitates the substantial movement of electrons from BiOCl to NO_2 gas. This occurrence of this phenomenon leads to the expansion of the depletion region, which in turn causes the sensor response to increase. This study provides new insight into room temperature ultrasensitive NO_2 gas sensors along with a low detection range for environmental and biomedical applications.

Conflicts of interest

The authors declare no conflicts of interest.

References

1 P. Kumari, N. Bahadur, L. Kong, L. A. O'Dell, A. Merenda and L. F. Dumée, Engineering Schottky-like and heterojunction materials for enhanced photocatalysis performance – A review, *Mater. Adv.*, 2022, **3**, 2309–2323, DOI: **10.1039/d1ma01062j**.

2 Y. Li, W. Li, Z. Jin, X. Luo, G. Xie, H. Tai, Y. Jiang, Y. Yang and Y. Su, Ternary ordered assembled piezoelectric composite for self-powered ammonia detection, *Nano Energy*, 2024, **122**, 109291, DOI: **10.1016/j.nanoen.2024.109291**.

3 H. Pan, G. Chen, Y. Chen, A. Di Carlo, M. A. Mayer, S. Shen, C. Chen, W. Li, S. Subramaniam and H. Huang, Biodegradable cotton fiber-based piezoresistive textiles for wearable biomonitoring, *Biosens. Bioelectron.*, 2023, **222**, 114999, DOI: **10.1016/j.bios.2022.114999**.

4 N. Basavaraj, A. Sekar and R. Yadav, Review on green carbon dot-based materials for the photocatalytic degradation of dyes: Fundamentals and future perspective, *Mater. Adv.*, 2021, **2**, 7559–7582, DOI: **10.1039/d1ma00773d**.

5 Z. Zhang, M. Xu, L. Liu, X. Ruan, J. Yan, W. Zhao, J. Yun, Y. Wang, S. Qin and T. Zhang, Novel SnO_2@ZnO hierarchical nanostructures for highly sensitive and selective NO_2 gas sensing, *Sens. Actuators, B*, 2018, **257**, 714–727, DOI: **10.1016/j.snb.2017.10.190**.

6 X. Ma, H. Zhu, L. Yu, X. Li, E. Ye, Z. Li, X. J. Loh and S. Wang, Rare-earth-doped indium oxide nanosphere-based gas sensor for highly sensitive formaldehyde detection at a low temperature, *Nanoscale*, 2022, **15**, 1609–1618, DOI: **10.1039/d2nr04972d**.

7 D. Simon Patrick, P. Bharathi, S. Kamalakannan, J. Archana, M. Navaneethan and M. Krishna Mohan, Confined oxidation of 2D WS_2 nanosheets forming WO_3/WS_2 nanocomposites for room temperature NO_2 gas sensing application, *Appl. Surf. Sci.*, 2024, **642**, 158554, DOI: **10.1016/j.apsusc.2023.158554**.

8 M. Hassan, Z. Liang, S. Liu, S. Hussain, G. Qiao and G. Liu, Temperature-driven n- to p-type transition of a chemiresistive NiO/CdS-CdO NO_2 gas sensor, *Sens. Actuators, B*, 2024, **398**, 134755, DOI: **10.1016/j.snb.2023.134755**.

9 C. Fan, J. Shi, Y. Zhang, W. Quan, X. Chen, J. Yang, M. Zeng, Z. Zhou, Y. Su, H. Wei and Z. Yang, Fast and recoverable NO_2 detection achieved by assembling ZnO on $Ti_3C_2T_x$ MXene nanosheets under UV illumination at room temperature, *Nanoscale*, 2022, **14**, 3441–3451, DOI: **10.1039/d1nr06838e**.

10 C. Chen, G. Xie, J. Dai, W. Li, Y. Cai, J. Li, Q. Zhang, H. Tai, Y. Jiang and Y. Su, Integrated core-shell structured smart textiles for active NO_2 concentration and pressure monitoring, *Nano Energy*, 2023, **116**, 108788, DOI: **10.1016/j.nanoen.2023.108788**.

11 J. Dai, G. Xie, C. Chen, Y. Liu, H. Tai, Y. Jiang and Y. Su, Hierarchical piezoelectric composite film for self-powered moisture detection and wearable biomonitoring, *Appl. Phys. Lett.*, 2024, **124**, 053701, DOI: **10.2139/ssrn.4515832**.

12 J. Ding, H. Dai, H. Chen, Y. Jin, H. Fu and B. Xiao, Highly sensitive ethylene glycol gas sensor based on ZnO/rGO nanosheets, *Sens. Actuators, B*, 2022, **372**, 132655, DOI: **10.1016/j.snb.2022.132655**.

13 X. Wang, X. Li, Y. Zhao, Y. Chen, J. Yu and J. Wang, The influence of oxygen functional groups on gas-sensing properties of reduced graphene oxide (rGO) at room temperature, *RSC Adv.*, 2016, **6**, 52339–52346, DOI: **10.1039/c6ra05659h**.

14 P. Duan, Q. Duan, Q. Peng, K. Jin and J. Sun, Design of ultrasensitive gas sensor based on self-assembled Pd-SnO_2/rGO porous ternary nanocomposites for ppb-level hydrogen, *Sens. Actuators, B*, 2022, **369**, 132280, DOI: **10.1016/j.snb.2022.132280**.

© 2024 The Author(s). Published by the Royal Society of Chemistry

Open Access Article. Published on 03 April 2024. Downloaded on 2/12/2026 8:17:39 AM. This article is licensed under a Creative Commons Attribution 3.0 Unported Licence.

15 D. Zhang, Z. Wu and X. Zong, Flexible and highly sensitive H_2S gas sensor based on in-situ polymerized SnO_2/rGO/PANI ternary nanocomposite with application in halitosis diagnosis, *Sens. Actuators, B*, 2019, **289**, 32–41, DOI: **10.1016/j.snb.2019.03.055**.

16 C. R. Minitha, V. S. Anithaa, V. Subramaniam and R. T. Rajendra Kumar, Impact of Oxygen Functional Groups on Reduced Graphene Oxide-Based Sensors for Ammonia and Toluene Detection at Room Temperature, *ACS Omega*, 2018, **3**, 4105–4112, DOI: **10.1021/acsomega.7b02085**.

17 J. Fan, L. Jiang, H. Lv, F. Qin, Y. Fan, J. Wang, M. Ikram and K. Shi, ZIF-67/BiOCl nanocomposites for highly efficient detection of NO_2 gas at room temperature, *J. Mater. Chem. A*, 2023, **11**, 15370–15379, DOI: **10.1039/d3ta01564e**.

18 L. Sun, L. Xiang, X. Zhao, C.-J. Jia, J. Yang, Z. Jin, X. Cheng and W. Fan, Enhanced Visible-Light Photocatalytic Activity of BiOI/BiOCl Heterojunctions: Key Role of Crystal Facet Combination, *ACS Catal.*, 2015, **5**, 3540–3551, DOI: **10.1021/cs501631n**.

19 M. Guerrero, A. Altube, E. Garcia-Lecina, E. Rossinyol, M. D. Baró, E. Pellicer and J. Sort, Facile in situ synthesis of BiOCl nanoplates stacked to highly porous TiO_2: a synergistic combination for environmental remediation, *ACS Appl. Mater. Interfaces*, 2014, **6**, 13994–14000, DOI: **10.1021/am5033549**.

20 Y. Yang, D. Zhang, D. Wang, Z. Xu and J. Zhang, A high-stability weighing paper/polytetrafluoroethylene-based triboelectric nanogenerator for self-powered In_2O_3 nanocubes/SnS_2 nanoflower NO_2 gas sensors, *J. Mater. Chem. A*, 2021, **9**, 14495–14506, DOI: **10.1039/D1TA03739K**.

21 M. Kumari, N. Dhariwal, V. Kumar and O. P. Thakur, Synthesis of p-$LaFeO_3$–n-$BaTiO_3$ heterojunctions and their room temperature methanol sensing applications, *IEEE Sens. J.*, 2023, **23**, 10301–10307, DOI: **10.1109/JSEN.2023.3263622**.

22 M. González-Garnica, A. Galdámez-Martínez, F. Malagón, C. D. Ramos, G. Santana, R. Abolhassani, P. Kumar Panda, A. Kaushik, Y. K. Mishra, T. V. K. Karthik and A. Dutt, One dimensional Au-ZnO hybrid nanostructures based CO_2 detection: Growth mechanism and role of the seed layer on sensing performance, *Sens. Actuators, B*, 2021, **337**, 129765, DOI: **10.1016/j.snb.2021.129765**.

23 S. Kumar, S. D. Lawaniya, S. Agarwal, Y.-T. Yu, S. R. Nelamarri, M. Kumar, Y. K. Mishra and K. Awasthi, Optimization of Pt nanoparticles loading in ZnO for highly selective and stable hydrogen gas sensor at reduced working temperature, *Sens. Actuators, B*, 2023, **375**, 132943, DOI: **10.1016/j.snb.2022.132943**.

24 Y. Zhong, W. Li, X. Zhao, X. Jiang, S. Lin, Z. Zhen, W. Chen, D. Xie and H. Zhu, High-Response Room-Temperature NO_2 Sensor and Ultrafast Humidity Sensor Based on SnO_2 with Rich Oxygen Vacancy, *ACS Appl. Mater. Interfaces*, 2019, **11**, 13441–13449, DOI: **10.1021/acsami.9b01737**.

25 X. Duan, D. Xu, W. Jia, B. Sun, R. Li, R. Yan and W. Zhao, Pt and black phosphorus co-modified flower-like WS_2 composites for fast NO_2 gas detection at low temperature, *Nanoscale*, 2024, **16**, 2478–2489, DOI: **10.1039/D3NR05424A**.

26 S. Maeng, S.-W. Kim, D.-H. Lee, S.-E. Moon, K.-C. Kim and A. Maiti, SnO_2 Nanoslab as NO_2 Sensor: Identification of the NO_2 Sensing Mechanism on a SnO_2 Surface, *ACS Appl. Mater. Interfaces*, 2014, **6**, 357–363, DOI: **10.1021/am404397f**.

27 Q. Li, D. Chen, J. Miao, S. Lin, Z. Yu, Y. Han, Z. Yang, X. Zhi, D. Cui and Z. An, Ag-Modified 3D Reduced Graphene Oxide Aerogel-Based Sensor with an Embedded Microheater for a Fast Response and High-Sensitive Detection of NO_2, *ACS Appl. Mater. Interfaces*, 2020, **12**, 25243–25252, DOI: **10.1021/acsami.9b22098**.

28 H. Zhang, L. Wang and T. Zhang, Reduced graphite oxide/SnO_2/Au hybrid nanomaterials for NO_2 sensing performance at relatively low operating temperature, *RSC Adv.*, 2014, **4**, 57436–57441, DOI: **10.1039/C4RA10474A**.

29 N. Sharma, H. S. Kushwaha, S. K. Sharma and K. Sachdev, Fabrication of $LaFeO_3$ and rGO-$LaFeO_3$ microspheres based gas sensors for detection of NO_2 and CO, *RSC Adv.*, 2020, **10**, 1297–1308, DOI: **10.1039/C9RA09460A**.

30 Q. Hao, T. Liu, J. Liu, Q. Liu, X. Jing, H. Zhang, G. Huang and J. Wang, Controllable synthesis and enhanced gas sensing properties of a single-crystalline WO_3–rGO porous nanocomposite, *RSC Adv.*, 2017, **7**, 14192–14199, DOI: **10.1039/C6RA28379A**.

31 J. Hao, D. Zhang, Q. Sun, S. Zheng, J. Sun and Y. Wang, Hierarchical SnS_2/SnO_2 nanoheterojunctions with increased active-sites and charge transfer for ultrasensitive NO_2 detection, *Nanoscale*, 2018, **10**, 7210–7217, DOI: **10.1039/c8nr01379a**.

32 S. Radhakrishnan and C. S. Rout, Recent developments in 2D MXene based materials for next generation room temperature NO_2 gas sensors, *Nanoscale Adv.*, 2023, **5**, 4649–4669, DOI: **10.1039/D3NA00275F**.

33 Y. L. Dong, X. F. Zhang, X. L. Cheng, Y. M. Xu, S. Gao, H. Zhao and L. H. Huo, Highly selective NO_2 sensor at room temperature based on nanocomposites of hierarchical nanosphere-like α-Fe2O3 and reduced graphene oxide, *RSC Adv.*, 2014, **4**, 57493–57500, DOI: **10.1039/c4ra10136g**.

34 U. V. Patil, C. S. Rout and D. J. Late, Impedimetric humidity sensor based on α-Fe_2O_3 nanoparticles, *Adv. Dev. Mater.*, 2015, **1**, 88–92, DOI: **10.1080/20550308.2015.1133101**.

35 P. Yadav, N. Dhariwal, M. Kumari, V. Kumar and O. P. Thakur, Enhanced degradation of Congo-red dye by Cr^{3+} doped α-Fe_2O_3 nano-particles under sunlight and industrial wastewater treatment, *Chemosphere*, 2023, **343**, 140208, DOI: **10.1016/j.chemosphere.2023.140208**.

36 A. R. Abdirakhmanov, A. Abdoli-Arani, R. Abel, F. Abid, A. E. Abrameshin, D. A. Abrameshin, J. Adabi, S. Aditya, M. A. Afanasyeva, S. K. Agarwal and M. Aghaei, *IEEE Trans. Plasma Sci.*, 2018, **46**, 4111–4208, DOI: **10.1109/TPS.2019.2891845**.

37 L. Phor, S. Chahal and V. Kumar, Zn^{2+} substituted superparamagnetic $MgFe_2O_4$ spinel-ferrites: Investigations on structural and spin-interactions, *J. Adv. Ceram.*, 2020, **9**, 576–587, DOI: **10.1007/s40145-020-0396-3**.

38 K. A. Mohammed, A. D. Al-Rawas, A. M. Gismelseed, A. Sellai, H. M. Widatallah, A. Yousif, M. E. Elzain and

© 2024 The Author(s). Published by the Royal Society of Chemistry

Open Access Article. Published on 03 April 2024. Downloaded on 2/12/2026 8:17:39 AM.
This article is licensed under a Creative Commons Attribution 3.0 Unported Licence.

M. Shongwe, Infrared and structural studies of $Mg_{1-x}Zn_x$-Fe_2O_4 ferrites, *Phys. B*, 2012, **407**, 795–804, DOI: 10.1016/j.physb.2011.12.097.

39 N. Dhariwal, P. Yadav, M. Kumari, P. Jain, A. Sanger, V. Kumar and O. P. Thakur, Iron Oxide-Based Nanoparticles for Fast-Response Humidity Sensing, Real-Time Respiration Monitoring, and Noncontact Sensing, *IEEE Sens. J.*, 2023, **23**, 22217–22224, DOI: 10.1109/JSEN.2023.3306475.

40 L. Phor and V. Kumar, Self-cooling by ferrofluid in magnetic field, *SN Appl. Sci.*, 2019, **1**, 1696, DOI: 10.1007/s42452-019-1738-z.

41 N. Dhariwal, M. Chahar, V. Kumar and O. P. Thakur, Ethanol sensing materials and device using Co^{2+}, Zn^{2+}, Cr^{2+} doped α-Fe_2O_3 nano-particles with room temperature response/recovery, *Sens. Actuators, B*, 2023, **390**, 134037, DOI: 10.1016/j.snb.2023.134037.

42 Z. Ye, H. Tai, R. Guo, Z. Yuan, C. Liu, Y. Su, Z. Chen and Y. Jiang, Excellent ammonia sensing performance of gas sensor based on graphene/titanium dioxide hybrid with improved morphology, *Appl. Surf. Sci.*, 2017, **419**, 84–90, DOI: 10.1016/j.apsusc.2017.03.251.

43 S. K. Abdel-Aal and A. S. Abdel-Rahman, Graphene influence on the structure, magnetic, and optical properties of rare-earth perovskite, *J. Nanopart. Res.*, 2020, **22**, 267, DOI: 10.1007/s11051-020-05001-7.

44 A. Gaur, P. Chand, J. Shah and R. K. Kotnala, Tin Oxide (SnO_2)-Decorated Reduced Graphene Oxide (rGO)-Based Hydroelectric Cells to Generate Large Current, *ACS Omega*, 2022, **7**, 43647–43656, DOI: 10.1021/acsomega.2c04553.

45 Y. Huang, X. Zhang and J. Zeng, Ternary heterojunctions catalyst of BiOCl nanosheets with the {001} facets compounded of Pt and reduced graphene oxide for enhancing photocatalytic activity, *J. Mater. Sci.: Mater. Electron.*, 2021, **32**, 2667–2684, DOI: 10.1007/s10854-020-04758-w.

46 Z. Li, Y. Qu, K. Hu, M. Humayun, S. Chen and L. Jing, Improved photoelectrocatalytic activities of BiOCl with high stability for water oxidation and MO degradation by coupling rGO and modifying phosphate groups to prolong carrier lifetime, *Appl. Catal., B*, 2017, **203**, 355–362, DOI: 10.1016/j.apcatb.2016.10.045.

47 S. Zhao, M. Li, M. Han, D. Xu, J. Yang, Y. Lin, N. E. Shi, Y. Lu, R. Yang, B. Liu, Z. Dai and J. Bao, Defect-Rich Ni_3FeN Nanocrystals Anchored on N-Doped Graphene for Enhanced Electrocatalytic Oxygen Evolution, *Adv. Funct. Mater.*, 2018, **28**, 1706018, DOI: 10.1002/adfm.201706018.

48 L. Tian, J. Liu, C. Gong, L. Ye and L. Zan, Fabrication of reduced graphene oxide-BiOCl hybrid material via a novel benzyl alcohol route and its enhanced photocatalytic activity, *J. Nanopart. Res.*, 2013, **15**, 1917, DOI: 10.1007/s11051-013-1917-6.

49 J. Sun, L. Sun, N. Han, H. Chu, S. Bai, X. Shu, R. Luo and A. Chen, rGO decorated CdS/CdO composite for detection of low concentration NO_2, *Sens. Actuators, B*, 2019, **299**, 126832, DOI: 10.1016/j.snb.2019.126832.

50 J. Pan, W. Liu, L. Quan, N. Han, S. Bai, R. Luo, Y. Feng, D. Li and A. Chen, Cu_2O and rGO Hybridizing for Enhancement of Low-Concentration NO_2 Sensing at Room Temperature, *Ind. Eng. Chem. Res.*, 2018, **57**, 10086–10094, DOI: 10.1021/acs.iecr.8b01430.

51 Y. Su, W. Li, X. Cheng, Y. Zhou, S. Yang, X. Zhang, C. Chen, T. Yang, H. Pan, G. Xie, G. Chen, X. Zhao, X. Xiao, B. Li, H. Tai, Y. Jiang, L. Q. Chen, F. Li and J. Chen, High-performance piezoelectric composites via β phase programming, *Nat. Commun.*, 2022, **13**, 4867, DOI: 10.1038/s41467-022-32518-3.

52 X. Wang, X. Yao, H. Bai and Z. Zhang, Oxygen vacancy-rich 2D GO/BiOCl composite materials for enhanced photocatalytic performance and semiconductor energy band theory research, *Environ. Res.*, 2022, **212**, 113442, DOI: 10.1016/j.envres.2022.113442.

53 Y. Wang, J. Wu, Z. Liu, H. Wang, J. Zhang and N. Li, Construction of BiOCl/reduced graphene oxide nanocomposites heterojunction with abundant oxygen vacancies for efficient photocatalytic organic pollutant removal, https://ssrn.com/abstract=4639112.

54 Q. Ma, Y. Shu, Z. Ding, L. Cao, X. Chen and F. Yang, Effect of chromium doping on the structure and band gap of Bi3.15Nd0.85Ti3O12 thin films, *J Alloys Compd.*, 2018, **768**, 847–851, DOI: 10.1016/j.jallcom.2018.07.307.

55 Z. Wang, J. Sun, Y. Huo, Y. Yan, Z. Ma, M. Bu, C. Sun, Z. Hua, X. Yang, W. Bi and T. Zhang, Porous Co_3O_4 nanocrystals derived by metal-organic frameworks on reduced graphene oxide for efficient room-temperature NO_2 sensing properties, *J. Alloys Compd.*, 2021, **856**, 158199, DOI: 10.1016/j.jallcom.2020.158199.

56 N. Song, H. Jiang, T. Cui, L. Chang and X. Wang, Synthesis and enhanced gas-sensing properties of mesoporous hierarchical α-Fe_2O_3 architectures from an eggshell membrane, *Micro Nano Lett.*, 2012, **7**, 943–946, DOI: 10.1049/mnl.2012.0631.

57 M. Tonezzer, Selective gas sensor based on one single SnO_2 nanowire, *Sens. Actuators, B*, 2019, **288**, 53–59, DOI: 10.1016/j.snb.2019.02.096.

58 M. U. Khan, G. Hassan, M. Awais and J. Bae, All printed full range humidity sensor based on Fe_2O_3, *Sens. Actuators, A*, 2020, **311**, 112072, DOI: 10.1016/j.sna.2020.112072.

59 J. Y. Patil, D. Y. Nadargi, J. L. Gurav, I. S. Mulla and S. S. Suryavanshi, Glycine combusted $ZnFe_2O_4$ gas sensor: Evaluation of structural, morphological and gas response properties, *Ceram. Int.*, 2014, **40**, 10607–10613, DOI: 10.1016/j.ceramint.2014.03.041.

60 Q. Zhang, G. Xie, M. Duan, Y. Liu, Y. Cai, M. Xu, K. Zhao, H. Tai, Y. Jiang and Y. Su, Zinc Oxide Nanorods for Light-Activated Gas Sensing and Photocatalytic Applications, *ACS Appl. Nano Mater.*, 2023, **6**, 17445–17456, DOI: 10.1021/acsanm.3c02403.

61 X. Song, L. Li, X. Chen, Q. Xu, B. Song, Z. Pan, Y. Liu, F. Juan, F. Xu and B. Cao, Enhanced triethylamine sensing performance of α-Fe_2O_3 nanoparticle/ZnO nanorod heterostructures, *Sens. Actuators, B*, 2019, **298**, 126917, DOI: 10.1016/j.snb.2019.126917.

62 J. P. Cheng, B. B. Wang, M. G. Zhao, F. Liu and X. B. Zhang, Nickel-doped tin oxide hollow nanofibers prepared by electrospinning for acetone sensing, *Sens. Actuators, B*, 2014, **190**, 78–85, DOI: 10.1016/j.snb.2013.08.098.

© 2024 The Author(s). Published by the Royal Society of Chemistry

Open Access Article. Published on 03 April 2024. Downloaded on 2/12/2026 8:17:39 AM.
This article is licensed under a Creative Commons Attribution 3.0 Unported Licence.

63 B. Jiang, W. Tao, L. Zhao, T. Wang, X. Liu, F. Liu, X. Yan, Y. Sun, G. Lu and P. Sun, Gas Sensing with Double-Shell Zno Hollow Microspheres Prepared by Template-Free Method, Available at SSRN 4084757 (2022). , DOI: **10.2139/ssrn.4084757**.

64 K. V. Sopiha, O. I. Malyi, C. Persson and P. Wu, Chemistry of Oxygen Ionosorption on SnO_2 Surfaces, *ACS Appl. Mater. Interfaces*, 2021, **13**, 33664–33676, DOI: **10.1021/acsami.1c08236**.

65 O. Lupan, F. Schütt, V. Postica, D. Smazna, Y. K. Mishra and R. Adelung, Sensing performances of pure and hybridized carbon nanotubes-ZnO nanowire networks: A detailed study, *Sci. Rep.*, 2017, **7**, 14715, DOI: **10.1038/s41598-017-14544-0**.

66 V. V. Sysoev, J. Goschnick, T. Schneider, E. Strelcov and A. Kolmakov, A Gradient Microarray Electronic Nose Based on Percolating SnO_2 Nanowire Sensing Elements, *Nano Lett.*, 2007, **7**, 3182–3188, DOI: **10.1021/nl071815**.

67 J. Z. Ou, W. Ge, B. Carey, T. Daeneke, A. Rotbart, W. Shan, Y. Wang, Z. Fu, A. F. Chrimes, W. Wlodarski, S. P. Russo, Y. X. Li and K. Kalantar-zadeh, Physisorption-Based Charge Transfer in Two-Dimensional SnS_2 for Selective and Reversible NO_2 Gas Sensing, *ACS Nano*, 2015, **9**, 10313–10323, DOI: **10.1021/acsnano.5b04343**.

68 Z. Chen, J. Wang, D. Pan, Y. Wang, R. Noetzel, H. Li, P. Xie, W. Pei, A. Umar, L. Jiang, N. Li, N. F. de Rooij and G. Zhou, Mimicking a Dog's Nose: Scrolling Graphene Nanosheets, *ACS Nano*, 2018, **12**, 2521–2530, DOI: **10.1021/acsnano.7b08294**.

69 R. Guo, Y. Han, C. Su, X. Chen, M. Zeng, N. Hu, Y. Su, Z. Zhou, H. Wei and Z. Yang, Ultrasensitive room temperature NO_2 sensors based on liquid phase exfoliated WSe_2 nanosheets, *Sens. Actuators, B*, 2019, **300**, 127013, DOI: **10.1016/j.snb.2019.127013**.

70 R. Kumar, N. Goel and M. Kumar, UV-Activated MoS_2 Based Fast and Reversible NO_2 Sensor at Room Temperature, *ACS Sens.*, 2017, **2**, 1744–1752, DOI: **10.1021/acssensors.7b00731**.

71 M. Cheng, Z. Wu, G. Liu, L. Zhao, Y. Gao, B. Zhang, F. Liu, X. Yan, X. Liang, P. Sun and G. Lu, Highly sensitive sensors based on quasi-2D rGO/SnS_2 hybrid for rapid detection of NO_2 gas, *Sens. Actuators, B*, 2019, **291**, 216–225, DOI: **10.1016/j.snb.2019.04.074**.

72 C. Zou, J. Hu, Y. Su, Z. Zhou, B. Cai, Z. Tao, T. Huo, N. Hu and Y. Zhang, Highly repeatable and sensitive three-dimensional γ-Fe_2O_3@reduced graphene oxide gas sensors by magnetic-field assisted assembly process, *Sens. Actuators, B*, 2020, **306**, 127546, DOI: **10.1016/j.snb.2019.127546**.

73 S. Liu, B. Yu, H. Zhang, T. Fei and T. Zhang, Enhancing NO_2 gas sensing performances at room temperature based on reduced graphene oxide-ZnO nanoparticles hybrids, *Sens. Actuators, B*, 2014, **202**, 272–278, DOI: **10.1016/j.snb.2014.05.086**.

74 R. You, D.-D. Han, F. Liu, Y.-L. Zhang and G. Lu, Fabrication of flexible room-temperature NO_2 sensors by direct laser writing of In_2O_3 and graphene oxide composites, *Sens. Actuators, B*, 2018, **277**, 114–120, DOI: **10.1016/j.snb.2018.07.179**.

75 N. Chen, X. Li, X. Wang, J. Yu, J. Wang, Z. Tang and S. A. Akbar, Enhanced room temperature sensing of Co_3O_4-intercalated reduced graphene oxide based gas sensors, *Sens. Actuators, B*, 2013, **188**, 902–908, DOI: **10.1016/j.snb.2013.08.004**.

76 O. Leenaerts, B. Partoens, F. M. Peeters, A. Volodin and C. Van Haesendonck, The work function of few-layer graphene, *J. Phys.: Condens. Matter*, 2016, **29**, 035003, DOI: **10.1088/0953-8984/29/3/035003**.

77 Y.-R. Lin, W.-H. Cheng, M. H. Richter, J. S. DuChene, E. A. Peterson, C. M. Went, Z. Y. Al Balushi, D. Jariwala, J. B. Neaton, L.-C. Chen and H. A. Atwater, Band Edge Tailoring in Few-Layer Two-Dimensional Molybdenum Sulfide/Selenide Alloys, *J. Phys. Chem. C*, 2020, **124**, 22893–22902, DOI: **10.1021/acs.jpcc.0c04719**.

78 G. Qu, G. Fan, M. Zhou, X. Rong, T. Li, R. Zhang, J. Sun and D. Chen, Graphene-Modified ZnO Nanostructures for Low-Temperature NO_2 Sensing, *ACS Omega*, 2019, **4**, 4221–4232, DOI: **10.1021/acsomega.8b03624**.

79 G. Qu, G. Fan, M. Zhou, X. Rong, T. Li, R. Zhang, J. Sun and D. Chen, Graphene-Modified ZnO Nanostructures for Low-Temperature NO_2 Sensing, *ACS Omega*, 2019, **4**, 4221–4232, DOI: **10.1021/acsomega.8b03624**.

80 M. Ikram, H. Lv, Z. Liu, K. Shi and Y. Gao, Hydrothermally derived p–n MoS_2–ZnO from p–p MoS_2-ZIF-8 for an efficient detection of NO_2 at room temperature, *J. Mater. Chem. A*, 2021, **9**, 14722–14730, DOI: **10.1039/D1TA03578A**.

81 X. Meng, S. Tongay, J. Kang, Z. Chen, F. Wu, S.-S. Li, J.-B. Xia, J. Li and J. Wu, Stable p- and n-type doping of few-layer graphene/graphite, *Carbon*, 2013, **57**, 507–514, DOI: **10.1016/j.carbon.2013.02.028**.